Supporting Information

Soranno et al. 10.1073/pnas.1117368109

SI Text

SI Materials and methods. ***Protein preparation and labeling.*** Five different variants of Csp were prepared starting from a DNA sequence with an additional C-terminal cysteine (Table S1, CspC67). In contrast to the terminal positions, which are not influenced by quenching (1), previously published results on reconfiguration dynamics in the internal positions of Csp (2) were found to be affected by quenching of the FRET dyes by Trp side chains. Here we avoid this complication by replacing all Trp residues in the protein by Phe, which does not quench donor or acceptor (3). This lack of quenching is reflected by a more pronounced anticorrelation in the donor-acceptor cross-correlation functions (Fig. 1). The good agreement of the reconfiguration times obtained for the terminally labeled variant used here and the terminally labeled protein containing both Trp residues (1) (note that no fluorophore quenching is observed for the terminally labeled variant in both cases), indicates that the Trp to Phe exchanges do not affect unfolded state dynamics significantly. Several second cysteine residues were introduced by site-directed mutagenesis to provide specific labeling positions for the dyes (see Table S1 for all amino acid sequences). All variants were expressed with an N-terminal hexahistidine tag containing a tryptophan residue to facilitate detection and quantification by UV-Vis spectroscopy during purification. After purification, the proteins were digested with HRV 3C protease to cleave off the His-tag. The sequence CspC36C69 contains an additional protease cleavage site (Factor Xa) N-terminal to Cys36 for the preparation of a bisected variant that enables a comparison of the full length protein and the shortened peptide corresponding to the C-terminal segment alone. The synthetic starting gene (Celtek Bioscience) was cloned into vector pET47b (+). The variants were expressed in E. coli BL21 (DE3) and purified from the inclusion bodies using a HisTrap column (GE Healthcare, BioSciences AB) in 20 mM Tris-HCl, 0.5 M NaCl, 2 mM β-mercaptoethanol, 20 mM imidazole, 4 M GdmCl, pH 8.0 and elution with an imidazole gradient. The resulting protein was dialyzed against 50 mM sodium phosphate, 0.5 mM EDTA, 2 mM β-mercaptoethanol, pH 7.4 and digested by adding HRV 3C protease (containing a His-tag; 1mg HRV 3C per 55 mg Csp). Finally, digested Csp was separated from protease, uncleaved Csp, and free His-tag by a second HisTrap chromatography run. Labeling was performed as described previously (2, 4) and verified by mass spectrometry. IN and ProTα were expressed, purified, and labeled as described previously (5).

Single-molecule fluorescence spectroscopy. Single-molecule fluorescence measurements were performed with a MicroTime 200 confocal microscope (PicoQuant, Berlin, Germany) equipped with a diode laser (LDH-D-C-485, PicoQuant), a HeNe laser (594 nm, CWI Melles Griot) and an Olympus UplanApo 60x/1.20W objective (Olympus). Emitted photons were collected through the microscope objective, focused onto a 100 μm pinhole and then separated into four channels with a polarizing beam splitter and a dichroic mirror (585DCXR, Chroma). Photons emitted by the acceptor dye were additionally filtered (HQ650/100 Chroma Technology) and then focused onto a SPAD detector (Perkin Elmer). Photons emitted by the donor dye were filtered (ET525/50M, Chroma Technology) and detected with an avalanche photodiode (MPD, PDM series, 50 μm, PicoQuant). The arrival time of every detected photon was recorded by a HydraHarp 400 counting module (PicoQuant), and the time between excitation pulse and photon detection pulse was stored with 4 ps resolution (time resolution was thus limited by the timing jitter of the detectors).

The donor dye was excited with an average power of 100 μW. Single-molecule FRET efficiency histograms were acquired in samples with protein concentrations of about 20 pM to 50 pM; detected photons were recorded with a time resolution of 16 ps, with the laser in pulsed mode at a repetition rate of 64 MHz. Nanosecond-FCS measurements were performed in samples with a protein concentration of approximately 1 nM, with the laser in continuous wave mode, with typical data acquisition times of 10 to 16 h. Control measurements to determine the contribution of quenching to the acceptor intensity autocorrelation were carried out by exciting with a continuous wave HeNe laser (594 nm, CVI Melles Griot) at a power of 16 μW. All measurements were performed in 50 mM sodium phosphate buffer, pH 7.0, 150 mM β-mercaptoethanol, and 0.001% Tween 20 (Pierce) with varying concentrations of GdmCl. 20 mM cysteamine were added to enhance the fluorophore brightness and minimize bleaching.

Rapid mixing experiments were performed essentially as described by Hofmann et al. (6). Microfluidic mixers fabricated by replica molding in polydimethylsiloxane (PDMS) were used (6, 7). 200 pM of terminally labeled Csp unfolded in 1.5 M GdmCl from the inlet channel (from the left in Fig. 4*B*) were mixed with buffer without denaturant from the side channels (from the top and bottom in Fig. 4*B*), resulting in a final concentration of 0.25 M GdmCl in the observation channel (to the right in Fig. 4*B*). 0.015 % Tween 20 were included to prevent nonspecific interactions of the protein with the PDMS surfaces. Measurements were taken by placing the confocal volume at a position 50 μm (8 ms) downstream of the mixing region. The experiments were performed with pressures of 13.8 kPa (2.0 psi) applied to all channels. To estimate the time after mixing, the calculated average fully developed flow velocity of 1.2 mm/s (13.8 kPa) in the observation channel was corrected by accounting for the change in width of the observation channel from the mixing area to the observation point, as described by Pfeil et al. (7). The stability of the flow velocity during the measurements was confirmed by analyzing the donor-acceptor fluorescence intensity cross-correlation functions (8). nsFCS measurements were taken for 6 h and analyzed as described below (in *Nanosecond-FCS measurements*).

The viscosities of the solutions were measured with a digital viscometer (DV-I+, Brookfield Engineering) with a CP40 spindle and 30–60 rpm, which allows determination of viscosity with an uncertainty of 0.05 to 0.1 mPa s. The calibration of the instrument was tested with a reference solution of known viscosity. The changes in refractive index caused by the addition of viscogens and/or denaturant were determined with a digital Abbe refractometer (Krüss, Germany) and were taken into account for the calculation of the Förster radii for the corresponding solution conditions.

Data analysis. ***Fluorescence lifetimes and FRET efficiencies.*** The average fluorescence lifetimes were estimated as the mean detection time of the burst photons after donor excitation. The transfer efficiencies were obtained from $E = n_A/(n_A + n_D)$, where n_D and n_A are the numbers of donor and acceptor photons in the burst corrected for background, channel crosstalk, acceptor direct excitation, differences in quantum yields of the dyes, and detection efficiencies (9). For a fixed distance r, the mean donor lifetime in the presence of acceptor is given by $\tau_{DA} = \tau_{DA}(r) = \tau_D(1 - E(r))$, where τ_D is the lifetime in the absence of acceptor

and $E(r) = 1/(1 + R_0^6/r^6)$, with the Förster radius R_0 calculated for the respective values of the refractive index of the solution (10) (black straight line in Fig. 1*B*). For a chain with a probability density function $P(r)$ of the interdye distance r, $\tau_{DA} = \int_0^\infty tI(t)\mathrm{d}t / \int_0^\infty I(t)\mathrm{d}t$ with $I(t) = I_0 \int_0^\infty P(r)e^{-t/\tau_{DA}(r)}\mathrm{d}r$, where I is the time-dependent fluorescence emission intensity, and the mean FRET efficiency is calculated as $\langle E\rangle = \int_0^\infty E(r)P(r)\mathrm{d}r$. In Fig. 1*b*, a Gaussian chain distribution for the distances

$$P_{\mathrm{Gauss}}(r) = 4\pi r^2 \left(\frac{3}{2\pi\langle r^2\rangle}\right)^{3/2} e^{-\frac{3r^2}{2\langle r^2\rangle}}, \qquad \textbf{[S1]}$$

(where $\langle r^2\rangle$ is the mean squared end-to-end distance of the segment probed) and the distribution of distances for a worm-like chain (11, 12) were compared. The resulting parametric plots are shown as the curved solid line (Gaussian chain) and the curved dashed line (worm-like chain), respectively. For the Gaussian chain, the corresponding radius of gyration, R_g, can be calculated from $R_g^2 = \langle r^2\rangle/6$. This conversion is used for the inset of Fig. 5 (main text) and for Figs. S2 and S6. For calculating persistence lengths, l_p, (Fig. S5), we use $l_p = \langle r^2\rangle/2l_c$, where l_c is the contour length of the segment probed (13), with corrections for dyes and linkers, as described previously (4). The insensitivity of the result to the detailed model used for the distance distribution is largely due to the similarity of the shape of the different distributions around their mean values given the low persistence lengths relative to the contour lengths of the polypeptides investigated here (5). Note that the long-range reconfiguration times observed here are much greater than the fluorescence lifetimes of the dyes; the effect of chain dynamics on the observed transfer efficiencies is thus negligible (14).

Nanosecond-FCS measurements. Autocorrelation curves of acceptor and donor channels and cross-correlation curves between acceptor and donor channels were calculated from measurements as described previously (1, 2). The data were fit over a time window of 4 μs with

$$g_{ij}(\tau) = 1 + \frac{1}{N}(1 - c_{\mathrm{AB}}e^{-\frac{t-t_0}{\tau_{\mathrm{AB}}}})(1 + c_{\mathrm{CD}}e^{-\frac{t-t_0}{\tau_{\mathrm{CD}}}})(1 + c_T e^{-\frac{t-t_0}{\tau_T}}),$$
$$i, j = A, D, \qquad \textbf{[S2]}$$

where N is the mean number of molecules in the confocal volume. The three multiplicative terms describe the contribution to amplitude and timescale of photon antibunching (AB), chain dynamics (CD), and triplet blinking of the dyes (T). In the case of the Csp variants, the three correlation curves were fit globally with the same values of τ_{CD} and t_0 above 1.5 M GdmCl. The amplitude and the lifetime of the antibunching and triplet component were fit with a free independent decay component for each correlation curve. Triplet lifetimes show a systematic increase in the range between 2 μs and 4 μs as the GdmCl concentration increases from 0 M to 7 M. Below 1.5 M GdmCl, only the donor autocorrelation was taken into account due to a significant contribution from the native state in the acceptor autocorrelation. The same approach was used for IN due to the presence of static quenching in the acceptor under native conditions. In the case of ProTα, data were fit globally over the entire range of GdmCl concentrations.

An estimation of the errors for Csp data has been obtained performing a Bootstrap-method, randomly sampling 50 subdatasets from the original dataset and fitting them with the same model. The obtained results have been used to estimate a standard deviation error from the mean. The resulting correlation times, τ_{CD}, can be described in terms of diffusion on the potential of mean force that corresponds to the $P(r)$ determined from the FRET efficiencies and fluorescence lifetimes and then converted in the reconfiguration time of the polypeptide chain (1).

Global fit of viscosity dependence of τ_r. The viscosity-dependent reconfiguration times measured at different GdmCl concentrations (Fig. 2) were fit globally according to Eq. **2** and **3** with $(\tau_r)_{\mathrm{GdmCl}} = a \cdot \langle r^2\rangle_{\mathrm{GdmCl}}\eta/\eta_0 + (\tau_i)_{\mathrm{GdmCl}}$, where $\langle r^2\rangle_{\mathrm{GdmCl}}$ is the mean square end-to-end distance of the chain as determined from single-molecule FRET experiments at a given GdmCl concentration, $(\tau_i)_{\mathrm{GdmCl}}$ is the "dry" internal friction contribution at the same GdmCl concentration, and a is a proportionality constant common to all GdmCl concentrations. According to the Rouse model, a can be related to the diffusion coefficient D_0 of a chain segment through $a = \frac{N}{3\pi^2 D_0}$ (13). Assuming that N equals the number of Kuhn segments (including the contribution of dyes and linkers), we obtain a value of $D_0 = (0.73 \pm 0.03) \cdot 10^{-5}\,\mathrm{cm}^2/\mathrm{s}$, in a reasonable range for our segment size. The global fit describes the observed behavior at all the denaturant conditions well, as shown in Fig. 2, suggesting that if there is a contribution from "wet" friction, it would be the same irrespective of the solvent.

The viscosity dependences of the bisected variant of Csp at different GdmCl concentrations were fit globally as the data of the full length protein (Fig. S8). The global fit provides an estimate of the internal friction times, with 45 ± 4 ns, 29 ± 5 ns, and 12 ± 6 ns at 1.0 M, 2.0 M, and 6.0 M GdmCl, respectively. The proportionality constant a in the global fit was converted to diffusion coefficient of the elementary segment D_0 as explained for the full length variant. In this case, $D_0 = (0.7 \pm 0.2) \cdot 10^{-5}\,\mathrm{cm}^2/\mathrm{s}$, in excellent agreement with the value for the full length protein, suggesting that the model does not only provide the correct scaling with the mean squared end-to-end distance, but also the correct scaling with the length of the sequence.

Extended RIF model. The Rouse model with internal friction (RIF) assumes that a polymer chain obeys the following equations of motion:

$$-\xi_s \frac{d\mathbf{r}}{\mathrm{d}t} - \xi_i \mathbf{k}\frac{d\mathbf{r}}{\mathrm{d}t} - k_0\mathbf{k}\mathbf{r} + \mathbf{f}(t) = 0 \qquad \textbf{[S3]}$$

Here $\mathbf{r}$ is the vector whose components are the positions of the polymer beads, k_0 is the stiffness of the spring connecting two adjacent beads, ξ_s and ξ_i are, respectively, the solvent- and the internal friction coefficients, $\mathbf{f}(t)$ is a random force vector satisfying the appropriate fluctuation-dissipation relationship, and $\mathbf{k}$ is a dimensionless connectivity matrix such that $k_0\mathbf{k}$ is the stiffness (Hessian) matrix of the chain. Specifically, this matrix is tridiagonal:

$$\mathbf{k} = \begin{bmatrix} -1 & 1 & 0 & 0 & \dots \\ 1 & -2 & 1 & 0 & \dots \\ 0 & 1 & -2 & 1 & \dots \\ 0 & 0 & 1 & -2 & \dots \\ \dots & \dots & \dots & \dots & \dots \end{bmatrix}$$

These equations describe the Brownian dynamics of a linear chain of N beads with coordinates $\mathbf{r}_1, \mathbf{r}_2, \dots, \mathbf{r}_N$, connected by harmonic springs such that the total potential energy is given by

$$V_0 = \frac{k_0}{2}\sum_{n=2}^{N}(\mathbf{r}_n - \mathbf{r}_{n-1})^2 \qquad \textbf{[S4]}$$

The mathematical structure of RIF is such that both the chain's stiffness matrix and the "friction matrix" $\xi_i\mathbf{k}$ appearing in the second term of Eq. **S3** are proportional to the same

connectivity matrix. This results in a particularly simple eigenmode spectrum, where the presence of internal friction does not change the eigenmodes of the system (which remain identical to the Rouse modes), but shifts all of its characteristic times by a constant amount,

$$\tau^{(n)} = (\tau_{\text{Rouse}}/n^2) + \tau_i, \qquad n = 1, 2, \ldots \qquad \textbf{[S5]}$$

where $\tau_i = \xi_i/k_0$ is the timescale associated with internal friction, and

$$\tau_{\text{Rouse}} = \frac{\xi_s}{3\pi^2}\frac{N\langle|\mathbf{r}_N - \mathbf{r}_1|^2\rangle}{k_{\text{B}}T} \qquad \textbf{[S6]}$$

is the longest relaxation time of the Rouse chain without internal friction.

For a quantitative comparison between the RIF model and experimental data, however, it is necessary to include two additional effects that are not taken into account in the original RIF model: one is the experimentally observed chain compaction at low denaturant concentrations due to the change in solvent quality, and the other is the change in the dynamics induced by the FRET dyes and the connecting linkers. To mimic chain compaction, we introduced an additional central potential

$$V_c = \sum_n k_c r_n^2/2,$$

which effectively compresses the chain towards the coordinate origin. In support of this simple approach, a comparison of the Rouse model modified in this way with more realistic simulations of a bead-and-spring model that included collapse-inducing attractive interactions showed that the behavior of both the statistical and the dynamical properties of the two models is quantitatively the same, given the same degree of chain compaction. Here, chain compaction is quantified by the ratio of its root mean square end-to-distance to that of the same chain in the absence of any attractive interactions (Fig. S4).

The donor and the acceptor dyes were represented as beads linked to the rest of the chain via harmonic springs of stiffness k_l. When the donor (D) and the acceptor (A) beads are connected, respectively, to chain beads i and j, this interaction is represented by a potential of the form

$$V_l = (1/2)k_l(\mathbf{r}_D - \mathbf{r}_i)^2 + (1/2)k_l(\mathbf{r}_A - \mathbf{r}_j)^2$$

Without this modification, the present model reproduces all of the results of Ref. (15) in the limit of zero friction. It should be noted, however, that, in contrast to Ref. (15), which predicts the existence of a maximum in the segment length dependence of the reconfiguration time, such a maximum is neither predicted by the present model nor observed experimentally.

In the absence of internal friction, the dynamics of the system is described by a straightforward generalization of the Rouse model:

$$-\boldsymbol{\xi}\frac{d\mathbf{r}}{\text{dt}} - \mathbf{K}\mathbf{r} + \mathbf{f}(t) = 0$$

In addition to the coordinates of the chain beads, the vector $\mathbf{r}$ in this equation includes the coordinates of the donor bead and of the acceptor bead. $\mathbf{K}$ is the matrix of the second derivatives (Hessian) for the potential $V_0 + V_c + V_l$, $\boldsymbol{\xi}$ is a diagonal friction matrix, whose diagonal entries are the friction coefficients equal to ξ_s for each chain bead, ξ_A for the acceptor, and ξ_D for the donor. Finally, $\mathbf{f}$ is an appropriate random force vector. It is convenient to introduce a friction-scaled Hessian matrix $\tilde{\mathbf{K}}$, whose elements are given by $\tilde{K}_{ij} = K_{ij}/\sqrt{\xi_{ii}\xi_{jj}}$, and rescaled coordinates and forces, $\tilde{r}_i = r_i\sqrt{\xi_{ii}}$, $\tilde{f}_i = f_i/\sqrt{\xi_{ii}}$, in terms of which the equations of motion become

$$-\frac{d\tilde{\mathbf{r}}}{\text{dt}} - \tilde{\mathbf{K}}\,\tilde{\mathbf{r}} + \tilde{\mathbf{f}}(t) = 0 \qquad \textbf{[S7]}$$

As in the Rouse model, Eq. **S7** is solved by decomposing the dynamics into those of independent relaxation modes, each of which effectively obeys overdamped harmonic oscillator dynamics. Those modes $\tilde{\mathbf{u}}_n$ are the eigenvectors of the matrix $\tilde{\mathbf{K}}$ satisfying the relation:

$$\tilde{\mathbf{K}}\tilde{\mathbf{u}}^{(n)} = (1/\tau^{(n)})\tilde{\mathbf{u}}^{(n)} \qquad \textbf{[S8]}$$

where $\tau^{(n)}$ are the corresponding relaxation times. To estimate the effective reconfiguration time for the relative motion of the donor and the acceptor, consider the autocorrelation time of their relative distance, written as a linear combination of the relaxation modes:

$$\mathbf{r}_{DA} = \mathbf{r}_D - \mathbf{r}_A = \frac{\tilde{\mathbf{r}}_D}{\sqrt{\xi_D}} - \frac{\tilde{\mathbf{r}}_A}{\sqrt{\xi_A}} = \frac{\sum_n x^{(n)}\tilde{u}_D^{(n)}}{\sqrt{\xi_D}} - \frac{\sum_n x^{(n)}\tilde{u}_A^{(n)}}{\sqrt{\xi_A}}, \qquad \textbf{[S9]}$$

where $\tilde{u}_{D,A}^{(n)}$ is the component of the nth relaxation vector that corresponds to the donor(acceptor) coordinates. The corresponding reconfiguration time τ_{DA} is estimated from the autocorrelation function

$$\tau_{DA} = \frac{\int_0^\infty dt\langle\mathbf{r}_{DA}(0)\mathbf{r}_{DA}(t)\rangle}{\langle\mathbf{r}_{DA}^2(0)\rangle} \qquad \textbf{[S10]}$$

Note that, although the timescale defined by Eq. **S10** is not identical to the experimentally estimated reconfiguration timescale, comparison with simulations of FRET in more realistic polypeptide models shows that it adequately captures the dependence of reconfiguration times on the donor and acceptor positions (15).

Eq. **S10** can be evaluated using the equipartition theorem applied to the relaxation modes. Taking advantage of their statistical independence results in the following expression for the autocorrelation functions:

$$\langle x^{(n)}(0)x^{(m)}(t)\rangle = k_{\text{B}}T\tau^{(n)}e^{-t/\tau^{(n)}}\delta_{nm}, \qquad \textbf{[S11]}$$

where δ_{nm} is the Kronecker delta.

We have further assumed that, as in the original RIF model, internal friction increases each relaxation time by the same amount without affecting the structure of the eigenmodes:

$$\tau^{(n)} \to \tau^{(n)} + \tau_i \qquad \textbf{[S12]}$$

As a result, the time dependence of the correlation functions in Eq. **S11** becomes modified, but their equilibrium statistical properties are unchanged:

$$\langle x^{(n)}(0)x^{(m)}(t)\rangle = k_{\text{B}}T\tau^{(n)}e^{-\frac{t}{\tau^{(n)}+\tau_i}}\delta_{nm} \qquad \textbf{[S13]}$$

Combining Eqs. **S9**, **[S10]**, and **[S13]**, we finally obtain:

$$\tau_{DA} = \frac{\sum_n\left(\frac{\tilde{u}_A^{(n)}}{\sqrt{\xi_A}} - \frac{\tilde{u}_D^{(n)}}{\sqrt{\xi_D}}\right)^2(\tau^{(n)})^2}{\sum_n\left(\frac{\tilde{u}_A^{(n)}}{\sqrt{\xi_A}} - \frac{\tilde{u}_D^{(n)}}{\sqrt{\xi_D}}\right)^2\tau^{(n)}} + \tau_i \qquad \textbf{[S14]}$$

To fit experimental data, the model requires the following parameters: k_c, k_l, ξ_A, ξ_D, and τ_i.

The friction of the dye ξ_D can be estimated considering that a Kuhn segment in 6M GdmCl corresponds to about five amino acids resulting in a molecular mass (approximately 600 Da) similar to that of dye and linker (643 Da for Alexa488 and 820 Da for Alexa 594), such that we assume $\xi_D = \xi_A \approx \xi_s$. Fits performed with $\xi_D = 2\xi_s$ yield results that are indistinguishable within experimental uncertainty, indicating that variation of the parameter within reasonable bounds does not affect the conclusions. The dye spring constant k_l was estimated by optimizing the fit of the model to the equilibrium interdye distances obtained from FRET efficiency histograms for the variants labeled at different positions in 7 M GdmCl, where no internal friction is present and the proteins are maximally expanded. The resulting value of k_l was then used for all other fits. Note that without including the dyes and linkers explicitly, the theory predicts a rollover in the reconfiguration time as a function of segment length when $|i\text{-}j|$ approaches the total number of segments (15), which is not observed experimentally. The confining spring constant k_c was adjusted such that the change in dimensions obtained from FRET efficiency histograms at different GdmCl concentrations relative to the maximally expanded state in 7 M GdmCl was reproduced. In this way the only remaining free parameter is the internal friction time τ_i, which is obtained from fitting the model to the position dependence of the reconfiguration times (Fig. 3). The τ_i extracted with this procedure is given relative to the τ_s obtained by the model at the same GdmCl concentration. In order to compare this result with values of internal friction obtained from the viscosity dependence, the ratio $\left(\frac{\tau_i}{\tau_{ij,(i=1,j=67)}}\right)_{\text{positiondependence}}$ was multiplied by the corresponding measured reconfiguration time of the end-to-end variant, τ_r, obtained at the same GdmCl concentration. Note that the uncertainty of τ_i determined in this way increases for large values of τ_i (Fig. 4) because the deviation of τ_{ij}/τ_r from a value of 1 becomes comparable to the experimental error.

Comparison of the effects of specific and nonspecific collapse on the chain dynamics. It could be argued that simple polymer models applied to unfolded proteins, especially under near-native conditions, are too unrealistic as they fail to capture the formation of partial secondary structure or specific hydrophobic clusters within the chain. Here we use simulations to argue (1) that experimental data can be used to differentiate nonspecific collapse assumed by such models from structural ordering and (2) that our experimental results, even at the lowest denaturant concentrations, where the conditions are close to native, are more consistent with the nonspecific collapse scenario. Specifically, we have simulated a variant of the generalized Rouse model (GRM) of Thirumalai and coworkers (16, 17) to mimic the formation of specific structural order within a chain by introducing an attractive interaction between an individual pair of monomers. An example of such a computation (Fig. S7) shows that the chain segment length dependence of both the intramonomer distance $r_{ij} = \langle|\mathbf{r}_j - \mathbf{r}_i|^2\rangle^{1/2}$ and reconfiguration time τ_{ij} found for a chain with attractive interactions between an individual pair of monomers is qualitatively different from both our experimental findings and from simple polymer models that assume nonspecific collapse. This finding suggests that specific structural ordering at low denaturant concentrations cannot explain our experimental results.

1. Nettels D, Gopich IV, Hoffmann A, Schuler B (2007) Ultrafast dynamics of protein collapse from single-molecule photon statistics. *Proc Natl Acad Sci USA* 104:2655–2660.
2. Nettels D, Hoffmann A, Schuler B (2008) Unfolded protein and peptide dynamics investigated with single-molecule FRET and correlation spectroscopy from picoseconds to seconds. *J Phys Chem B* 112:6137–6146.
3. Doose S, Neuweiler H, Sauer M (2005) A close look at fluorescence quenching of organic dyes by tryptophan. *Chemphyschem* 6:2277–2285.
4. Hoffmann A, et al. (2007) Mapping protein collapse with single-molecule fluorescence and kinetic synchrotron radiation circular dichroism spectroscopy. *Proc Natl Acad Sci USA* 104:105–110.
5. Müller-Späth S, et al. (2010) Charge interactions can dominate the dimensions of intrinsically disordered proteins. *Proc Natl Acad Sci USA* 107:14609–14614.
6. Hofmann H, et al. (2010) Single-molecule spectroscopy of protein folding in a chaperonin cage. *Proc Natl Acad Sci USA* 107:11793–11798.
7. Pfeil SH, Wickersham CE, Hoffmann A, Lipman EA (2009) A microfluidic mixing system for single-molecule measurements. *Rev Sci Instrum* 80:055105.
8. Gösch M, Blom H, Holm J, Rigler R (2000) Hydrodynamic flow profiling in microchannel structures by single molecule fluorescence spectroscopy. *Anal Chem* 72:3260–3265.
9. Schuler B (2007) Application of single molecule Förster resonance energy transfer to protein folding. *Methods Mol Biol* 350:115–138.
10. Kawahara K, Tanford C (1966) Viscosity and density of aqueous solutions of urea and guanidine hydrochloride. *J Biol Chem* 241:3228–3232.
11. Schuler B, Lipman EA, Steinbach PJ, Kumke M, Eaton WA (2005) Polyproline and the "spectroscopic ruler" revisited with single molecule fluorescence. *Proc Natl Acad Sci USA* 102:2754–2759.
12. Thirumalai D, Ha BY (1988) *Theoretical and Mathematical Models in Polymer Research*, ed Grosberg A (Academia, New York), pp 1–35.
13. Doi M, Edwards SF (1988) *The Theory of Polymer Dynamics* (Oxford University Press, USA, New York).
14. Nettels D, et al. (2009) Single molecule spectroscopy of the temperature-induced collapse of unfolded proteins. *Proc Natl Acad Sci. USA* 106:20740–20745.
15. Makarov DE (2010) Spatiotemporal correlations in denatured proteins: The dependence of fluorescence resonance energy transfer (FRET)-derived protein reconfiguration times on the location of the FRET probes. *J Chem Phys* 132:035104.
16. Barsegov V, Morrison G, Thirumalai D (2008) Role of internal chain dynamics on the rupture kinetic of adhesive contacts. *Phys Rev Lett* 100:248102.
17. Hyeon C, Morrison G, Thirumalai D (2008) Force-dependent hopping rates of RNA hairpins can be estimated from accurate measurement of the folding landscapes. *Proc Natl Acad Sci USA* 105:9604–9609.

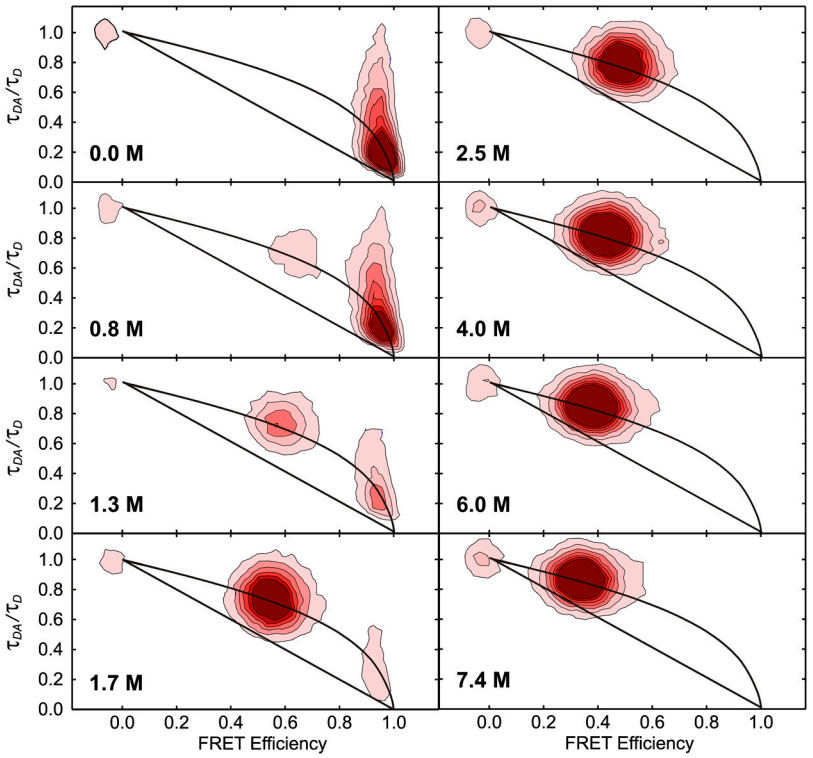

Fig. S1. Two-dimensional histograms of relative donor lifetime versus FRET efficiency measured between 0 M and 7.4 M GdmCl (cf. Fig. 1, main text). τ_{DA} and τ_D are the donor fluorescence lifetimes in presence and in absence of acceptor, respectively. For details, see *Fluorescence lifetimes and FRET efficiencies*.

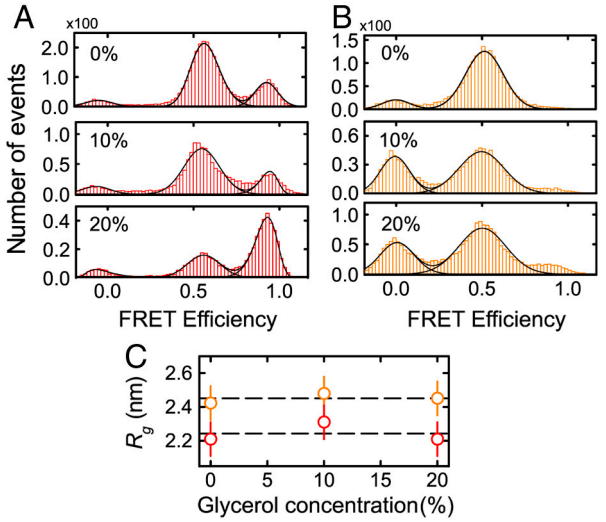

Fig. S2. FRET efficiency histograms of Csp at 1.3 M (*A*) and 2 M (*B*) GdmCl with different concentrations of glycerol (% by mass). At 1.3 M GdmCl and 20% glycerol, the denaturant concentration was adjusted slightly to 1.4 M GdmCl to counteract the effect of stabilization of the native state while maintaining the same transfer efficiency. Generally, the presence of glycerol in solution did not affect the radius of gyration of the chain significantly, as shown in (*C*) (colors as in *A*, *B*). The same behavior was observed at 4 M and 6 M GdmCl.

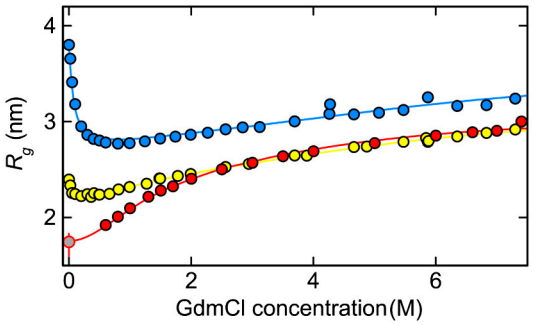

Fig. S3. Radii of gyration, R_g, for Csp (red), IN (yellow), and ProTα (blue) obtained assuming the distance distribution of a Gaussian chain. Very similar results are obtained with other distance distributions (5). The data for IN and ProTαC were fit as described previously (5). The expansion of IN and ProTα at low GdmCl concentration is due to charge repulsion at low ionic strength (5). For interpolation, the Csp data were fit with $R_g = R_{g0}(1 + \rho K_b a/(1 + K_b a))$, where R_{g0} is the dimension in the absence of denaturant, ρ is a scaling constant, K_b is an effective binding constant of denaturant to the chain, and a is the activity of the denaturant (5, 14). The residual difference in chain dimensions at high denaturant concentrations may be due to excluded volume effects from the long unlabeled polypeptide tail in ProTα or GdmCl binding to acidic side chains (5). The gray data point is from the microfluidic mixing experiment (see Fig. 4, main text).

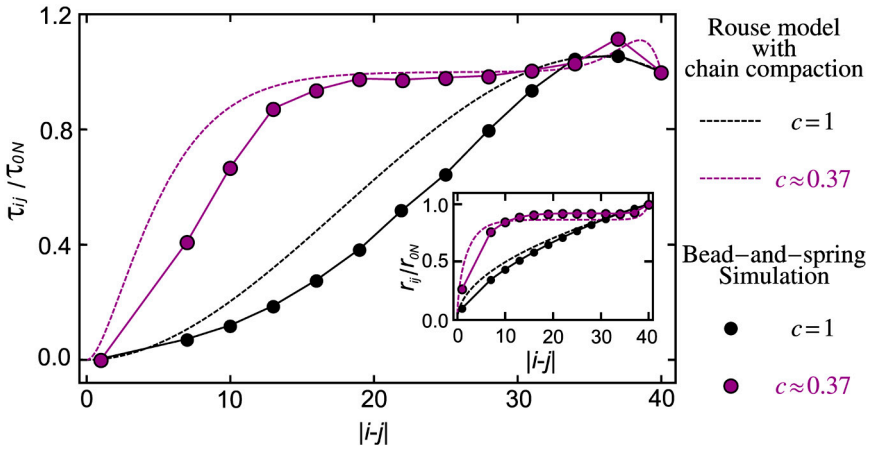

Fig. S4. Justification for using a simple harmonic potential to mimic chain collapse within the extended RIF. In the extended RIF, chain compaction is induced by applying a parabolic trapping potential to every chain monomer. Here we show that such a model realistically reproduces the properties of a chain undergoing a coil-to-globule transition. To simulate the coil-globule transition, we used a chain of $N = 41$ beads connected by harmonic springs. In addition, nonbonded beads interacted via a Lennard-Jones potential. Chain collapse was induced by lowering the temperature and quantified by the compactness parameter c equal to the ratio of the chain's root mean square distance to the root mean square distance corresponding to the high temperature limit (such that $c = 1$ at high temperature, in the absence of collapse). The reconfiguration time, τ_{ij}, and the rms distance, r_{ij}, plotted as a function of the length of the chain segment between the monomers i and j, agree well with those computed for a Rouse chain, in which collapse was introduced by applying a potential $k_c r^2/2$ to each monomer. Again, the degree of collapse for the Rouse chain was quantified by the compactness parameter c, taken, in this case, to be the ratio of the rms end-to-end distance to that for $k_c = 0$. Given the same values of the compactness parameter, the results for the Rouse model agree quite well with those for the bead-and-spring model, especially considering that the Rouse model does not take into account excluded volume effects. Here we only show the data for extreme cases of no compaction and very strong compaction (where c is smaller than the typical experimental values); similar agreement was observed for intermediate values of c (data not shown).

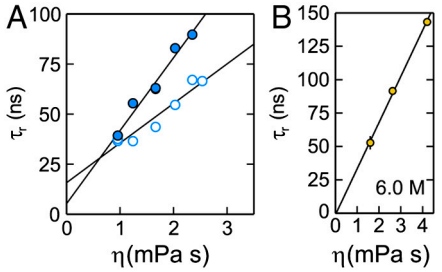

Fig. S5. (*A*) Viscosity dependence of the reconfiguration time of ProTα in native buffer (filled circles) and upon addition of 1 M KCl (empty circles). Data were fit globally as for the Csp viscosity dependence (Fig. 2), which resulted in values of the internal friction time of (6 ± 5) ns and (16 ± 3) ns without and with salt, respectively. (*B*) Viscosity dependence of the reconfiguration time of IN in 6 M GdmCl. The linear fit yields a value for the internal friction time of (-2 ± 6) ns, indicating that internal friction is negligible at high GdmCl concentrations.

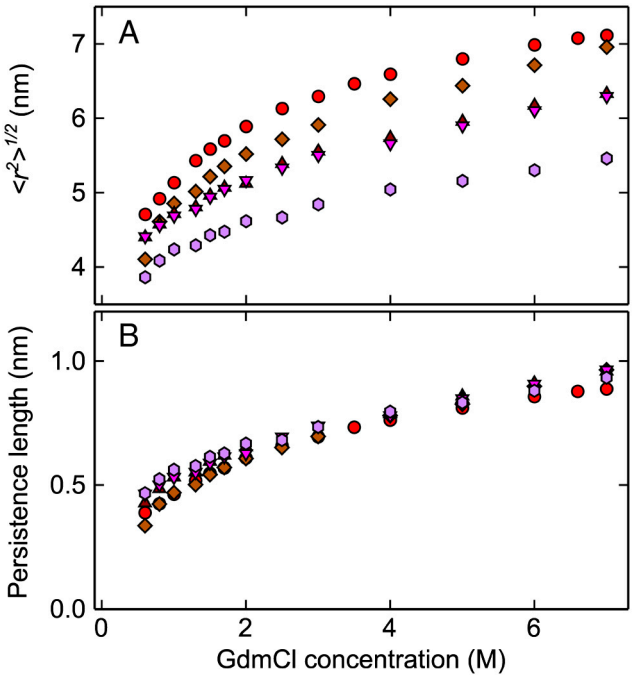

Fig. S6. Root mean squared interdye distances and persistence lengths as a function of GdmCl concentration for the different Csp variants (CspC2C68, red circles; CspC10C67 brown diamonds; CspC21C67, dark red triangles up; CspC22C67, pink triangles down; CspC36C69 violet hexagons). The good agreement of the persistence lengths indicates a uniform collapse of the chain (4) and thus the dominance of nonspecific interactions in driving collapse and causing internal friction.

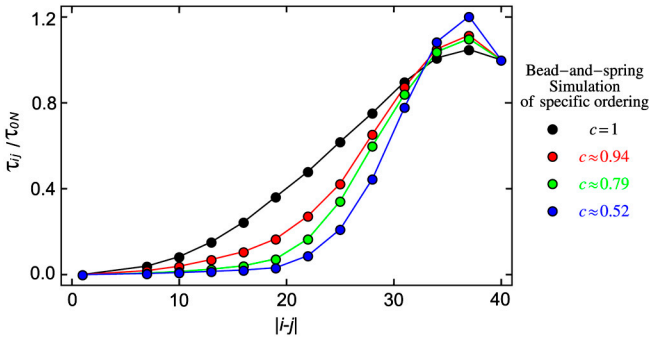

Fig. S7. Specific intrachain interactions result in spatio-temporal correlations within the polymer chain that are quite different from those observed experimentally and in simulations of nonspecific collapse. Here, we illustrate this using a generalized Rouse-type model (16, 17), in which a pair of monomers within a bead-and-spring chain model interact via an attractive potential. We use a chain with $N = 41$ beads, where the 4th and the 36th beads attract one another. We have also considered other choices of the two monomers (data not shown), leading to similar conclusions. As the strength of the attractive potential increases, more compact configurations are favored. Again, we characterize this compaction in terms of the compactness parameter c, equal to the ratio of the end-to-end distance and the end-to-end distance in the limit of no attractive interaction. The effect of chain compaction on the reconfiguration times τ_{ij} is very different from that observed in the experiments and in our simulations of chains without specific interactions (cf. Fig. S4). Specifically, more compact chains exhibit a τ_{ij} that decreases more precipitously with decreasing length of the chain segment $|i\text{-}j|$ between the monomers, in contrast to the weakening of this dependence observed experimentally at lower denaturant concentrations (Fig. 3) as well as predicted by the models that do not include monomer-specific interactions.

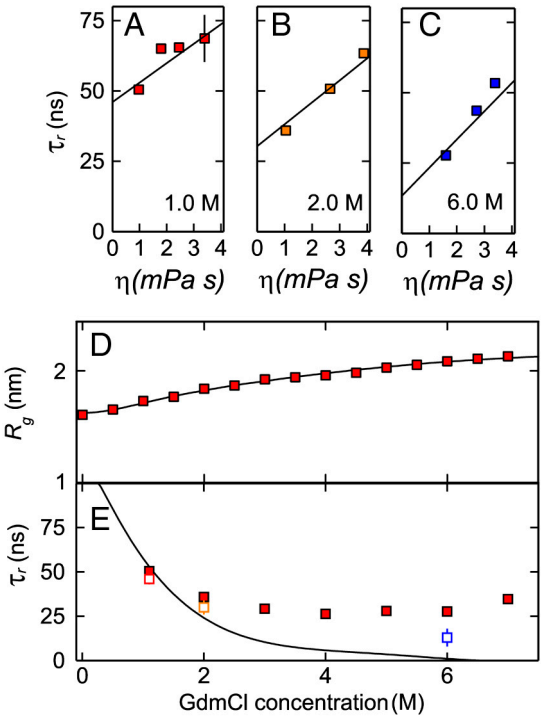

Fig. S8. Reconfiguration dynamics and internal friction of the bisected variant of CspC36C69 (see Tab. S1). Viscosity dependences of reconfiguration times, τ_r, at 1.0 M (*A*), 2.0 M (*B*), and 6.0 M GdmCl (*C*), respectively. The data were fit globally as in Fig. 2 (solid lines). (*D*) Denaturant dependence of the radius of gyration, R_g. (*E*) Reconfiguration times τ_r of the bisected variant (red filled squares) compared with the values of internal friction times obtained from the viscosity dependences (*A*–*C*) (empty squares, colors as in *A*–*C*), and with internal friction times of full length CspC2C68 (black line, from Fig. 4*A*). The good agreement of friction times in the two variants indicates the importance of local interactions for internal friction.

Table S1. Amino acid sequences of the variants of Csp from *Thermotoga maritima* used in this work (mutations relative to wt in bold, fluorophore labeling positions in bold underline)

		1 10 20 30 40 50 60
Csp(wild type)		MRGKVKWFDS KKGYGFITKD EGGDVFVHWS AIEMEGFKTL KEGQVVEFEI QEGKKGPQAA HVKVVE
CspC67	MAHHHHHHSWAALEVLFQ GPG	MRGKVK**F**FDS KKGYGFITKD EGGDVFVH**F**S AIEMEGFKTL KEGQVVEFEI QEGKKG**G**QAA HVKVVE**C**
CspC2C68	MAHHHHHHSWAALEVLFQ GPG	M**C**RGKVK**F**FD SKKGYGFITK DEGGDVFVH**F** SAIEMEGFKT LKEGQVVEFE IQEGKKG**G**QA AHVKVVE**C**
CspC10C67	MAHHHHHHSWAALEVLFQ GPG	MRGKVK**F**FD**C** KKGYGFITKD EGGDVFVH**F**S AIEMEGFKTL KEGQVVEFEI QEGKKG**G**QAA HVKVVE**C**
CspC21C67	MAHHHHHHSWAALEVLFQ GPG	MRGKVK**F**FDS KKGYGFITKD **C**GGDVFVH**F**S AIEMEGFKTL KEGQVVEFEI QEGKKG**G**QAA HVKVVE**C**
CspC22C67	MAHHHHHHSWAALEVLFQ GPG	MRGKVK**F**FDS KKGYGFITKD E**C**GDVFVH**F**S AIEMEGFKTL KEGQVVEFEI QEGKKG**G**QAA HVKVVE**C**
CspC36C69	MAHHHHHHSWAALEVLFQ GPG	MRGKVK**F**FDS KKGYGFITKD EGGDVFVH**F**S AIEGR**C**EGFK TLKEGQVVEF EIQEGKKG**G**Q AAHVKVVE**C**
CspC36C69 bisected		**C**EGFK TLKEGQVVEF EIQEGKKG**G**Q AAHVKVVE**C**

Proline was removed to eliminate a kinetic component due to cis/trans isomerization (2, 3, 16); Trp residues were replaced by Phe to eliminate static quenching of the internally labeled variants. The hexahistidine tag (blue) was removed by digest with HRV 3C protease. For CspC36C69 a Factor Xa protease site was introduced (underline) to allow preparation of a bisected variant lacking the N-terminal tail